Progression of creep deformation from grain boundaries to grain interior in Al-Cu-Mn-Zr alloys

J.U. Rakhmonov[1], B. Milligan[2,**], S. Bahl[2], D. Ma[3,***], A. Shyam[2,*] and D.C Dunand[1,*]

[1] Department of Materials Science & Engineering, Northwestern University, Evanston IL 60208, USA

[2] Materials Science and Technology Division, Oak Ridge National Laboratory, Oak Ridge, TN 37830, USA

[3] Chemical and Engineering Materials Division, Neutron Sciences Directorate, Oak Ridge National Laboratory, Oak Ridge, TN 37831, USA

* co-corresponding authors

** Presently at Pacific Northwest National Laboratory, Richland, WA 99354, USA

*** Presently at Songshan Lake Materials Laboratory, Dongguan 523800, China

Abstract

Creep mechanisms are studied in θ′-Al_2Cu-strengthened Al-Cu-Mn-Zr alloys at 300 and 350 °C for (i) ACMZ, a base alloy without further alloying elements and (ii) RR350, a commercial alloy with additions of Ni and Co forming distinct grain-boundary precipitates. At high stresses, creep is dominated by dislocations bypassing θ′ precipitates within grains via the Orowan mechanism, as evidenced by (ⅰ) very high stress exponent (n~20-25) and (ⅱ) α-Al and θ′ lattice strains (measured *via* in-situ neutron diffraction) evolving during creep in a manner consistent with *load transfer* from the plastically-deforming α-Al matrix to elastically-deforming θ′ precipitates. At intermediate stresses, both alloys exhibit a n~3 regime, where α-Al and θ′ lattice strains scale near-linearly with applied stress while remaining largely unaffected by strain accumulation, indicating that Orowan looping or dislocation pile-up around θ′ is now inactive within the grains. Rather, dislocation motion occurs solely in θ′-precipitate-free zones (θ′-PFZ) where high dislocation densities are observed via TEM after creep deformation. Plastic flow at θ′-PFZ and/or localized pipe diffusion are expected to enable grain-boundary sliding (GBS), which is proposed as the rate-limiting mechanism in the n~3 regime. Ni/Co-rich precipitates at RR350 grain-boundaries, with negligible θ′-PFZ around them, share load (as determined via neutron diffraction) with the α-Al matrix more effectively than θ-Al_2Cu precipitates at ACMZ grain-boundary, with wide surrounding θ′-PFZ. Thus, high creep resistance in

the *n*~3 GBS regime is enabled by coarsening-resistant grain-boundary precipitates, forming without concomitant development of weak θ′-PFZ, which effectively share load with the grains.

Keywords: Al-Cu alloys; θ′-precipitates; In-situ neutron diffraction; Creep; Grain-boundary precipitates; Load transfer.

1. Introduction

Interest in high-temperature Al-Cu-based alloys strengthened with θ′-(Al_2Cu) precipitates has grown substantially [1-9] following the discovery that the metastable θ′ phase can be stabilized up to 350 °C [10] by segregation of slow-diffusing solutes (e.g., Mn, Zr, Sc, and Fe) to the α-Al/θ′ interfaces [6, 10]. θ′-(Al_2Cu) precipitates have shown *no* measurable coarsening during exposure of Al-Cu-Mn-Zr alloy to 300 °C for 5000 h [11]. High coarsening resistance of θ′-(Al_2Cu) in this alloy at both 300 and 350 °C for 2100 h has been also demonstrated in Ref. [3]. The kinetic and thermodynamic factors which are responsible for such high coarsening resistance of θ′-(Al_2Cu) precipitates are well addressed in previous publications [2-5]. This discovery is a noticeable advance in the design of lightweight, cast Al-based alloys for high-temperature applications, given that (i) most other strengthening metastable precipitates - such as Ω (Al_2Cu), β″ (MgSi), η′ ($MgZn_2$) - formed in high-strength, precipitation-hardenable Al alloys rapidly coarsen and transform into undesirable, stable forms above 200-250 °C [12, 13] and (ii) the slow-diffusing transition metals that can form (meta-)stable and coarsening-resistant precipitates (e.g., Sc and Zr forming $L1_2$-Al_3(Sc,Zr)), also exhibit low solid solubility, thus resulting in much lower volume fraction of strengthening precipitates, with limited strengthening contribution [14, 15].

Several recent studies have focused on the creep response of Al-Cu alloys strengthened with stabilized θ′-precipitates, [3, 8, 16-19]. The creep behavior of these alloys has been characterized at 300 °C (a homologous temperature of ~0.60) at stresses higher than ~80 MPa, and found to be controlled by dislocation creep with the Orowan looping mechanism becoming the rate-limiting mechanism [3, 18]. However, the creep mechanisms prevailing at lower stresses (well below the Orowan stress), as well as the role of grain-boundary precipitates in the creep response of θ′-strengthened Al-Cu alloys require further research [3]. At stresses up to 20-30 MPa, diffusional creep - specifically Coble creep driven by vacancy diffusion along grain boundaries becomes rate-limiting, so that alloy microstructures with coarser grains exhibit lower creep strain rates as compared to alloys with finer grains [3, 19]. Ni/Co-rich intermetallic precipitates decorating grain boundaries, when present in large amounts (e.g., a volume-averaged fraction of ~6 vol.%), have also been found to strongly decrease diffusional creep rates, likely by inhibiting grain-boundary sliding (GBS) which is needed to accommodate diffusional creep [3, 19]; however, a similar fraction (~6 vol.%) of θ-Al_2Cu precipitates at grain boundaries of Al-Cu-Mn-Zr alloy with ~9 % Cu concentration does not reduce diffusional creep strain rates [16]. Moreover, Ni/Co-rich intermetallic phase, unlike θ-Al_2Cu at grain boundaries, have been found to reduce creep strain rates at higher stresses of up to 80 MPa (below Orowan stress), where the stress exponent *n* is close to three in compression, in a regime where the creep mechanism remains uncertain [3]. There is, therefore, a need for understanding the role of various grain-boundary precipitates on the creep response of Al-Cu alloys containing θ′-precipitates within their grains. This understanding, in turn, will allow the exploration of new pathways to design highly creep-resistant Al-Cu-based alloys. Lastly, no study exists in the literature concerning the creep behavior of θ′-strengthened Al-Cu alloys at 350 °C despite the coarsening- and transformation-resistance of these stabilized intragranular θ′ precipitates at this temperature [10].

Neutron diffraction (ND), owing to the high neutron penetration capability, can provide structural information from multiple grains/precipitates for each microstructural constituent [20]. ND performed in-situ on mechanically-loaded specimens allows to accurately determine elastic lattice

strains in differently oriented constituent phases under various loading conditions at ambient or elevated temperatures [21-23]. Time-resolved lattice strain evolution under loading allows a determination of the evolution of load sharing among various constituent phases during deformation. Given distinct elasto-plastic properties of matrix and precipitate phase, stresses partition between phases during deformation, and the evolution of this stress-sharing can be determined by in-situ ND measurements [24-26]. Although diffraction gives no information on the extent of plastic deformation experienced by each phase under loading, elastic strains in various phases provide a direct measurement of stresses in these phases, which can be compared to modeling predictions. As reported in Ref. [18], in-situ ND measurements during creep of θ′-strengthened Al-Cu alloys with Ni/Co-rich intermetallics precipitates at grain-boundaries were previously conducted at high stresses, where the Orowan looping mechanism dominates: it was demonstrated that load transfer from the plastically-deforming α-Al matrix to elastically-deforming θ′-precipitates within grains increases linearly with macrostrain. However, no in-situ ND measurements have been reported during long-term creep of this alloy at lower stresses (< 80 MPa), where (ⅰ) the Orowan looping mechanism is unlikely to be active [3] and (ⅱ) dislocation climb over high-aspect-ratio θ′ precipitates is also limited [18].

In this study, in-situ ND measurements during creep at 300 and 350 °C (homologous temperatures of 0.60 and 0.67) are performed on two cast Al-Cu-Mn-Zr alloys with similar intragranular Mn- and Zr-stabilized θ′-Al_2Cu precipitates but different grain-boundary precipitates (θ-Al_2Cu and Ni/Co-containing phases, respectively). These experiments shed light on: (ⅰ) the creep mechanisms dominating below the Orowan stress in the n~3 regime and (ⅱ) how creep deformation affects stress-partitioning between grain-boundary precipitates, their associated precipitate-free zones, and the θ′-strengthened grain interiors. Also, creep tests without concomitant ND are conducted at 350 °C to explore the operating creep mechanisms and the role of grain-boundary precipitates at this higher temperature.

2. Experimental Procedures

2.1 Material fabrication

Table 1 provides the chemical composition of the two cast Al-Cu-Mn-Zr and Al-Cu-Ni-Co-Mn-Zr-Sb alloys investigated in this study, hereafter labeled ACMZ and RR350 (its commercial name), respectively. ACMZ can be considered a simplified version of RR350, with similar amounts of Cu, Mn, and Zr , but without Ni and Co which form distinct grain-boundary precipitates together with Fe and Cu, and without small addition of Sb (present in RR350 for better castability [27]). Castings from both alloys were produced by pouring the melt, fully homogenized at 800 °C, into a wedge-shaped semi-permanent mold, with iron chills closest to their narrow end.

Table 1. Chemical composition of ACMZ and RR350 alloys (wt. %).

	Cu	Mn	Zr	Fe	Si	Ni	Co	Ti	Sb	Al
ACMZ	6.4	0.19	0.13	0.1	0.05	-	-	0.09	-	bal.
RR350	4.8	0.19	0.17	0.09	0.05	1.2	0.26	0.21	0.15	bal.

Specimens from both ACMZ and RR350 alloys were machined from the narrowest section of the wedge-casting to obtain fine-grained structures (with average grain diameter of ~ 43 and 57 μm, respectively). Specimens were then subjected to T7 heat treatment which was followed by preconditioning treatment for 200 h at 300 °C to stabilize microstructure, including θ′ precipitates, prior to creep exposure. The T7 treatment parameters were as follows: (ⅰ) solution treatment for 5 h at 540 °C for ACMZ and at 535 °C for RR350, (ⅱ) quenching in water at ~ 80 °C and (ⅲ) aging to form θ′ precipitates, for 5 h at 240 °C for ACMZ and 4 h at 220 °C for RR350.

2.2 In-situ neutron diffraction during creep

In-situ time-of-flight (TOF) neutron diffraction (ND) measurements of the (hkl)-specific lattice strain evolutions for various constituent phases of ACMZ and RR350 alloys during creep deformation were carried out on the VULCAN beamline at Oak Ridge National Laboratory, Spallation Neutron Source (ORNL, SNS) [25]. Threaded dog-bone specimens, with a gauge-length of 50 mm and a diameter of 6.35 mm, were mounted in a MTS load frame, with macroscopic engineering strain measured with a high-temperature extensometer with 10 mm gauge-length directly attached to the gauge section. Creep tests for in-situ ND measurements were conducted by both multi-step loading (~20-105 MPa) at 300 °C and single-step loading at 300 and 350 °C. During multi-step loading, a single specimen was crept under a series of increasing stresses, with each creep period lasting at least 8 h. During single-step loading, separate specimens were used for creep tests at a given stress and temperature, and experiments lasted ~12 h or until rupture. Specimen heating was carried out by induction coils positioned around the specimen after its installation in the load frame. Temperature of the specimen was monitored and controlled using two K-type thermocouples spot-welded at its middle section.

Neutron diffraction spectra were continuously recorded during creep by two ±90° detectors, allowing to measure lattice strains along loading and transversal directions from the scattering volume [25]. For simplicity, only lattice strain evolutions parallel to the loading direction are reported in this study. Neutron diffraction data collected during the test were chopped and binned into 20-min or 30-min segments, depending on the creep exposure period, with 5 min overlaps on both ends, performed to improve the intensity of the peaks, particularly those from constituent phases with low volume fraction. The hkl-specific lattice strain is calculated as $\epsilon_{hkl} = (d^{hkl} - d_0^{hkl})/ d_0^{hkl}$ [25], where d^{hkl} is the hkl-specific interplanar spacing measured under load at test temperature for a binned segment and where d_0^{hkl} is the hkl-specific spacing measured at test temperature prior to applying the load. ND data reduction and single-peak fitting were carried out using VULCAN's data analysis software – VDRIVE [25] - to determine hkl-specific lattice strains.

2.3 Ex-situ creep testing

Creep tests were conducted by multi-step loading (~10-85 MPa) using a lever-arm creep frame at 350 °C in compression on preconditioned (350 °C/200h) specimens with ~10 mm diameter and ~22 mm length. Specimen temperature was monitored using K-type thermocouple attached to it. Linear variable differential transformer (LVDT) with 10 µm resolution, installed on the cold end of an extensometer, was used to measure creep strain in the specimen. Two specimens per alloy were tested to ascertain reproducibility of the creep behavior.

2.4 Microstructure investigation

Alloy microstructure before and after creep tests was examined using scanning electron microscopy (SEM, FEI Quanta 650) and transmission electron microscopy (TEM, JEOL ARM 200CF). Specimens for SEM observations were prepared by standard mounting, grinding and polishing procedures, with the final polishing step conducted using colloidal silica to reach ~ 60 nm surface roughness. TEM thin foils were obtained by mechanical grinding of a disk with 3 mm diameter until its thickness reaches ~ 100 µm followed by Twin-Jet electropolishing at 20 V DC in an electrolyte (25% nitric acid and 75% methanol) maintained at -27 ± 5 °C.

3. Results

3.1 Microstructures prior to creep deformation

Microstructures of alloys investigated in this study - cast Al-Cu-Mn-Zr (ACMZ) and Al-Cu-Mn-Zr alloy with Ni (and Co) additions (RR350) - have been previously investigated in depth [3]. Here, their

major microstructural differences are briefly highlighted in Fig. 1. The TEM micrograph in Fig.1a shows platelet-shaped θ′ (metastable Al_2Cu) precipitates distributed in the α-Al matrix of ACMZ; the θ′ structure of RR350 (not provided here) is similar, except for a slightly lower volume fraction commensurate with a lower copper content in the latter alloy [3]. However, major differences exist in the grain-boundary precipitates of these alloys. ACMZ has ~2 vol.% of equilibrium θ (Al_2Cu) precipitates located at grain-boundaries and formed predominantly during solidification and some formed during subsequent aging and conditioning (with much finer size). By contrast, RR350 has ~6 vol.% of Ni-rich precipitates (Al_7Cu_2(Ni,Fe) and Al_9FeNi), with much higher aspect ratio than the θ-precipitates, which are all residing at grain boundaries and interdendritic regions, and are expected to have formed on solidification [3]. Moreover, as discussed previously [3] and shown here in Fig. 1b,c (insets), θ′-precipitate-free zones (θ′-PFZ) are wider around θ precipitates located at grain boundaries, and therefore, ACMZ has much higher θ′-PFZ volume as compared to RR350. The distribution of θ′-PFZ along grain boundaries in ACMZ and RR350 can be also seen in supplementary Fig. S1 (a and b, respectively).

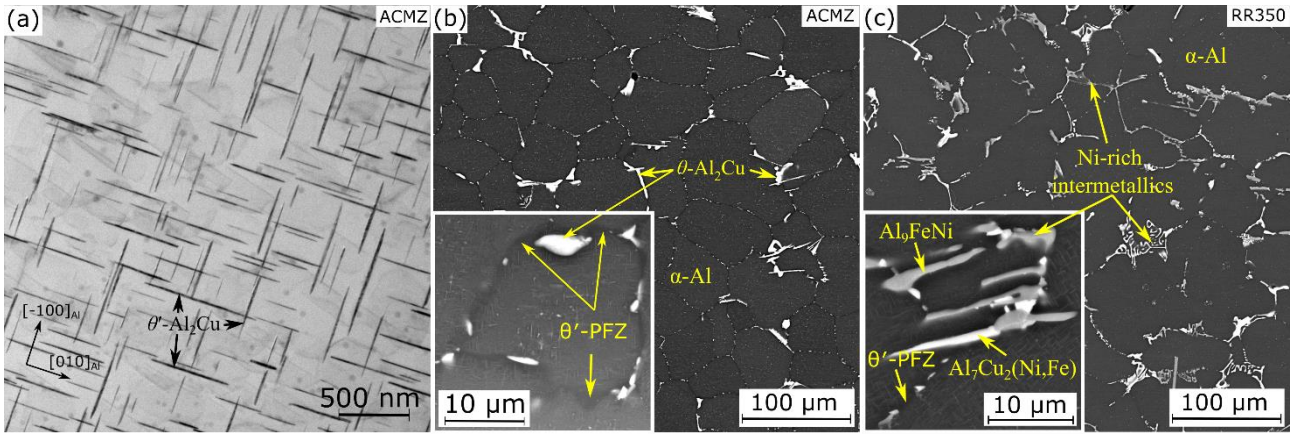

Fig. 1. (a) Bright-field TEM micrograph, acquired near $[001]_{Al}$ zone axis in 2-beam condition, showing distribution of platelet-shaped θ′ precipitates in the α-Al matrix; (b,c) low-magnification SEM micrographs showing the distribution and morphology of grain boundary precipitates (b) θ (Al_2Cu) in ACMZ and (c) Al_7Cu_2(Ni,Fe) and Al_9FeNi in RR350. Inserts in (b) and (c) show the distribution of θ′-precipitate-free zones (θ′-PFZ) along/near grain boundaries in ACMZ and RR350, respectively.

3.2 Macroscopic-creep behavior

Figure 2 displays, for ACMZ and RR350 tested at 300 and 350 °C, a logarithmic plot of the minimum strain rate $\dot{\varepsilon}$ against applied stress σ, consistent with the modified Norton creep power-law [28]:

$$\dot{\varepsilon} = K\sigma^n \exp[-\frac{Q_c}{RT}] \quad (1)$$

where K is a material constant, n is the stress exponent, Q_c is the creep activation energy and RT is the thermal energy. Creep properties of both ACMZ and RR350 have been previously investigated at 300 °C in both tension and compression, as reported in Refs. [3, 19]. Compressive creep data obtained previously from ex-situ tests (without ND measurements) at 300 °C for these alloys are also displayed in Fig. 2a, in addition to tensile creep data from in-situ tests (ND measurements during creep) at 300 °C, from the current study. Given the lack of literature creep data for these alloys at 350 °C, despite the confirmed stability of strengthening θ′ precipitates at 350 °C for lengthy periods in ACMZ alloy [10], additional ex-situ compressive creep tests at 350 °C on these alloys were conducted, with results shown in Fig. 2b. Tensile creep data, obtained at 350 °C from in-situ tests, are also included in Fig. 2b for comparison. In tension, cavitation along grain boundaries increases both strain rate and the

stress exponent *n* as compared to compressive testing, where cavitation does not occur [3, 29]; thus, compressive creep data from ex-situ tests provide stress exponent *n* value which better represent the creep deformation mechanism.

At 300 °C, appreciable difference exists between strain rates from (previously investigated) ex-situ tests and current in-situ tests, at any given stress below ~ 75 MPa (Fig. 2a). This difference suggests that samples were deforming primarily in the primary creep regime for in-situ tests. Fig. S2 displays strain evolution curves vs. time at two different stresses for RR350 from in-situ tests. Clearly, the creep exposure time is too short at 34 MPa to achieve a steady-state regime (Fig. S2). At 78 MPa, by contrast, clearly defined primary and secondary creep regimes are observed, due to a longer creep exposure time (Fig. S2). Moreover, at high stresses (> 75 MPa), as strain rates are faster and thus times to reach steady-state strain rate are shorter, similar values of secondary strain rates during both in- and ex-situ tests are achieved. By comparison with creep data from previous ex-situ tests, the creep regimes of these alloys at 300 °C can be interpreted as follows. At low stresses (< 30 MPa), diffusional creep, with vacancy diffusion along grain boundaries, i.e., Coble creep, becomes rate-limiting for both alloys; the higher fraction of intermetallic precipitates which extensively decorate grain boundaries of RR350, as compared to ACMZ, results in reduced diffusional creep rates [3, 19]. At intermediate stresses (30 – 85 MPa), a stress exponent n~3 is measured for both alloys, but the corresponding creep mechanism remains unclear, as the obtained *n* value is below that for the dislocation climb of pure Al (n=4-5) [30] and as dislocation climb over high-aspect-ratio θ′ precipitates has been demonstrated to be limited [18]. At high stresses (> 85 MPa), the *n* value increases significantly to ~20-24, which has been associated with the activation of glide with the Orowan looping mechanism [3, 17, 18], as expected from the θ′ precipitates being predominantly non-shearable [31]. Understanding the creep mechanism at intermediate stresses in the n~3 regime (below the Orowan stress) and determining the role of grain-boundary precipitates in the creep response of the alloys are critical to reveal new pathways to further enhance creep resistance of Al-Cu alloys.

At 350 °C, as shown in Fig. 2b, the creep strength is predictably lower than at 300 ºC, but many similarities exist: (i) for both alloys, at lower stresses (below 55-60 MPa), a n~3 regime exists, with RR350 exhibiting much lower strain rates (by about an order of magnitude) as compared to ACMZ; (ii) at higher stresses, the stress exponent increases drastically (n~20) and the creep resistance of both alloys becomes similar. These observations imply that the same creep mechanism dominates at both 300 and 350 °C for each of the two creep regimes (n~3 and n~20-24), and it is likely that a diffusional creep regime also exists at 350 ºC, at stresses below 20 MPa for RR350 and at or just below the lowest tested stress of 15 MPa for ACMZ. Also included in Fig. 2b are the creep data from in-situ tensile tests at 350 °C for these alloys. Clearly, the measured strain rates for each alloy are higher as compared to those obtained in compression; this discrepancy is again explained by the short creep time during in-situ tests, which are insufficient to achieve a steady-state strain rate. Moreover, as observed for these alloys in a previous study [3], tensile creep also activates cavitation at/along grain boundaries, which is another creep mechanism that contributes to the strain rate and increases the *n* value, but remains inactive in compression.

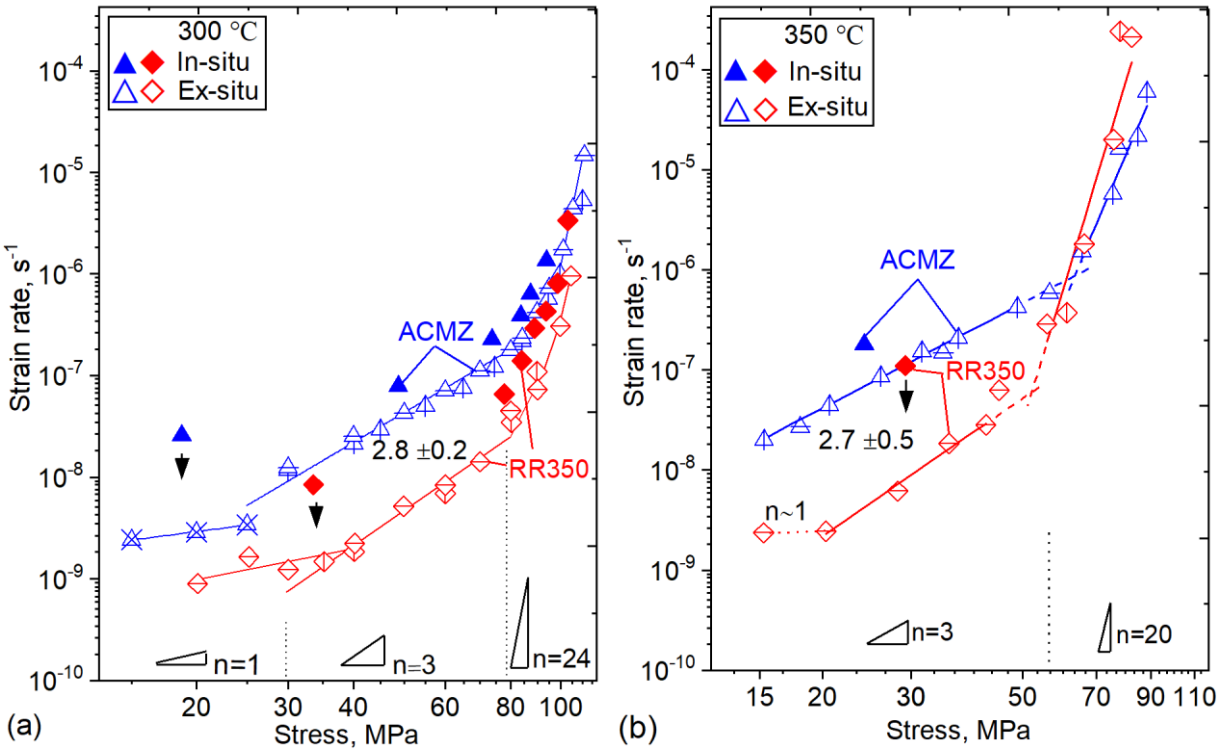

Fig. 2. Double-logarithmic plots of creep strain rates as function of applied stress for ACMZ and RR350 alloys in compression (open symbols) or tension (closed symbols) at (a) 300 ºC and (b) 350 °C. Tensile creep data are obtained from in-situ creep tests (with ND measurements) and compressive creep data are from ex-situ creep experiments (without ND measurements), as reported in Ref. [3] at 300 °C and as measured in the present study at 350 °C. Differently oriented lines within the same symbols represent the creep data from different specimens for a given alloy.

3.3 In-situ neutron diffraction measurements during creep

3.3.1 Neutron diffraction pattern

Fig. 3 displays neutron diffraction spectra acquired for RR350 and ACMZ at 300 °C without loading. Four peaks from various crystallographic planes of α-Al (i.e., (311), (220), (200) and (111)) are used to track lattice strain evolution during creep; these peaks are well developed and clearly defined for both alloys (Fig. 3). The only peak from θ′ that does not overlap with those from other precipitates is (211) for both alloys (Fig. 3a). This $(211)_{\theta'}$ peak remains well-defined for alloys crept at both 300 and 350 °C (not reported here). For θ precipitates existing primarily at grain boundaries of ACMZ (Fig. 1b), two (310) and (220) peaks (Fig. 3a) are used to track lattice strain evolution during creep. For RR350, in which Ni-rich intermetallic phases extensively decorate grain boundaries (Fig. 1c), the (303) and (602) peaks for $Al_7Cu_2(Ni,Fe)$ are used.

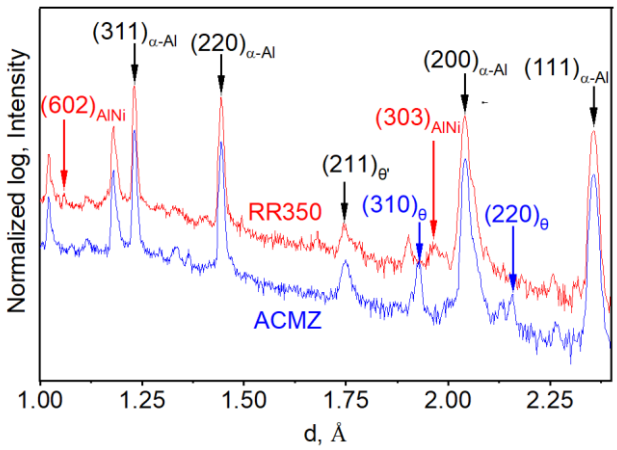

Fig. 3. Neutron diffraction spectra for ACMZ and RR350 alloys, acquired at 300 °C prior to tensile creep loading, showing the 9 peaks, from the 4 constituent phases, selected to measure lattice strain evolution during subsequent creep loading. AlNi refers to $Al_7Cu_2(Ni,Fe)$ phase in RR350.

3.3.2 (hkl) plane-specific lattice strain evolution during multi-step loading creep

Figures 4a and d display the temporal evolutions of the (hkl) plane-specific lattice strains along the loading direction for differently oriented α-Al grains of ACMZ and RR350, respectively, at selected stresses. For both alloys, the (200), (220), (311) and (111) α-Al lattice strains are nearly identical at various stresses, as exemplarily shown for ACMZ at 19 MPa (Fig. 4a) and RR350 at 34 MPa (Fig. 4d). The (311) α-Al lattice strain is known to represent the average macroscopic strain for FCC metals [32], and therefore, the lattice strain for this orientation is used in this study to describe the α-Al lattice strain changes during various creep conditions. Increasing the stress up to ~75-80 MPa (above which the stress exponent *n* changes from ~3 to ~24 in Fig. 2a), in a stress range referred to as *low-stress region* in this study, increases α-Al lattice strain. However, increasing the stress beyond ~75-80 MPa (referred to as *high-stress region*) results in marginal lattice strain increase in α-Al (Fig. 4a,d). Also, the α-Al lattice strain remains largely constant with creep time in the *low-stress region*, whereas, at higher stresses, the α-Al lattice strain tends to decline with creep time (Fig. 4a,d).

Figure 5a,b displays the α-Al lattice strain (averaged over the full creep time for a given stress) as function of the applied stress for both alloys. Between 19 and 75-80 MPa in the *low-stress region*, the α-Al lattice strain increases linearly with stress, with a slope of ~60 GPa for both ACMZ and RR350, respectively: these values are close to the Young's modulus of Al at 300 ºC, which is ~45-50 GPa [33]. At stresses higher than ~75-80 MPa (Fig. 5a,b), the slope increases sharply (and even becomes negative beyond ~ 100 MPa for RR350), indicating that the matrix stress increases less than expected from a purely elastic response (and is even slightly unloaded beyond ~ 100 MPa for RR350). This behavior is consistent with the α-Al matrix plastically deforming by creep in the *high-stress region* and transferring load to the other constituent phases, as discussed below.

For the θ′ phase present within the grains of both alloys, the (211) θ′ lattice strain increases linearly with applied stress, while remaining near constant with creep time, in the *low-stress region*, as shown in Fig. 4b,e. However, in the *high-stress region*, the θ′ lattice strain increases noticeably both with stress and creep time. As apparent from Fig. 5a,b, the (211) θ′ lattice strain increases with stress near linearly in the *low-stress region*; for ACMZ between 18 and 74 MPa, the slope of the stress-strain curve for the θ′ phase (Fig. 5a) is the same as for the α-Al matrix, suggesting that both θ′ and α-Al deform elastically in iso-strain manner, preventing any elastic load transfer. In the *high-stress region*, this increase in lattice strain becomes much more pronounced with stress; the larger standard deviations at high stresses is due to the θ′ lattice strain increasing with creep time (Fig. 5a,b). These results imply that: (i) θ′ continues to deform elastically, and not plastically, at even the highest

applied stresses and (ii) plastic deformation of the α-Al matrix in the *high-stress region* is largely responsible for a significant increase in θ′ elastic lattice strain. The strong increase in θ′ lattice strain, which occurs along with a slight α-Al lattice strain decrease in the *high-stress region*, is a clear indication of load transfer from the plastically-deforming α-Al matrix to elastically-deforming θ′ precipitates. The higher the stress level is, the stronger the increase in θ′ lattice strain with creep time (Fig. 5). Still, the θ′ lattice strain increases linearly with macrostrain (Fig. S3), which is consistent with increasing back-stresses due to accumulation of Orowan dislocation loops or piled-up dislocations around θ′ precipitates [18, 34].

Turning now to the θ phase in ACMZ alloy, as shown in Fig. 4c, lattice strain increases only slightly with stress, while showing significant fluctuations with creep time. This increase in lattice strain over the stress range is much smaller for the θ phase than for the α-Al and θ′ phases (Fig. 4c vs. Fig. 4a,b and Fig. 5a), suggesting that the α-Al matrix does not effectively share load with the θ precipitates during creep. By contrast, the lattice strain of the Ni-rich grain-boundary phase in RR350 (as represented by (602) plane of $Al_7Cu_2(Ni,Fe)$ displays a more pronounced increase with stress, reaching lattice strain levels exceeding that of α-Al (but much lower than that of the intergranular θ′ phase). Comparing Figs. 4c and 4f, and Figs. 5a and 5b, it is apparent that the Ni-rich grain-boundary precipitates in RR350 exhibit higher lattice strains (i.e., carry much higher stresses) than the grain-boundary θ precipitates in ACMZ. In other words, load transfer from the α-Al matrix to the grain-boundary precipitates is more efficient in RR350 than in ACMZ.

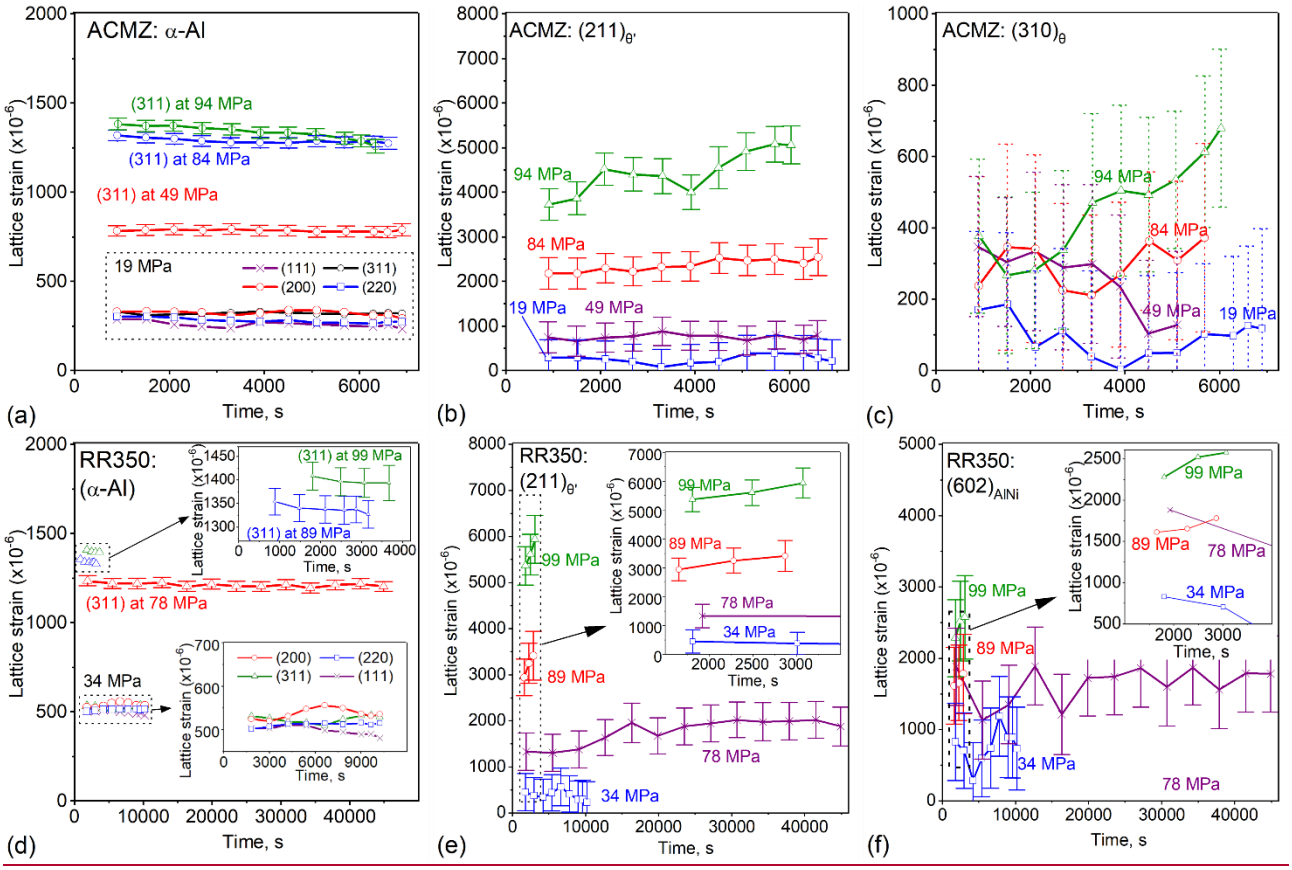

Fig. 4. Temporal evolution of (hkl) plane-specific lattice strains for various constituent phases (α-Al, θ-Al_2Cu, θ′-Al_2Cu, AlNi ($Al_7Cu_2(Ni,Fe)$) at several applied stresses, obtained from in-situ neutron diffraction measurements during creep at 300ºC of (a-c) ACMZ and (d-f) RR350 alloys. Fitting errors associated with the measured lattice strains for some conditions are provided.

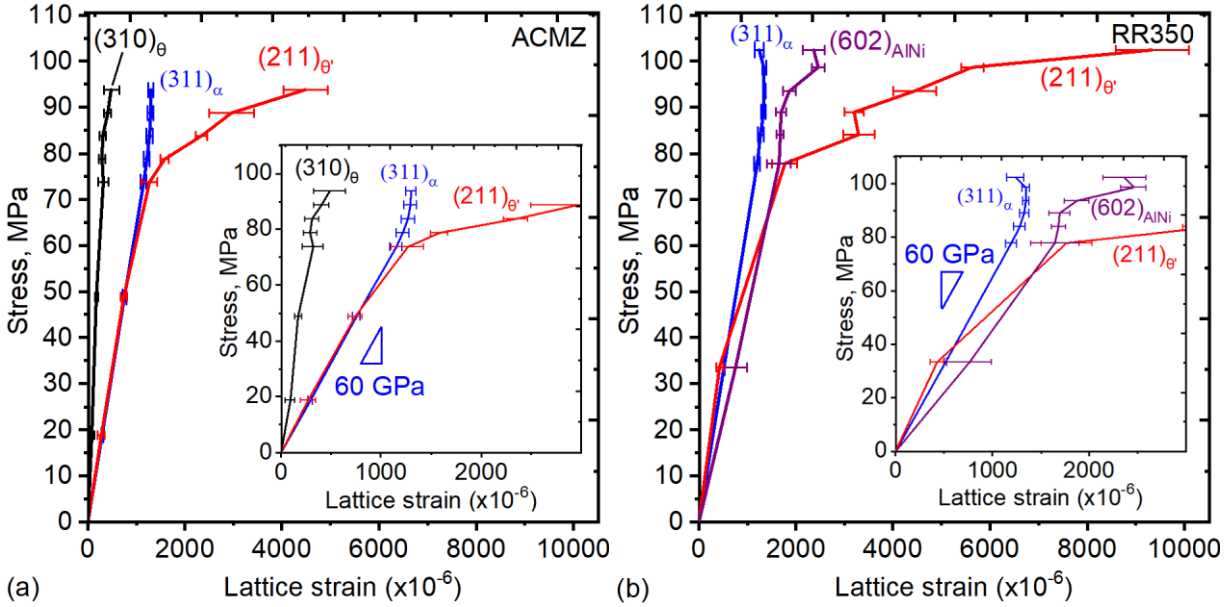

Fig. 5. Relationship between applied stress and (hkl) plane-specific average lattice strain (averaged for a given stress) for various constituent phases (α-Al, θ-Al_2Cu, θ′-Al_2Cu, AlNi ($Al_7Cu_2(Ni,Fe)$), obtained from in-situ neutron diffraction measurements during multi-step creep at 300 ºC of (a) ACMZ and (b) RR350 alloys.

3.4 (hkl) plane-specific lattice strain evolution during single-step loading creep

Fig. 6a,b shows the evolution of the (hkl) plane-specific lattice strains for α-Al, θ and θ′ phases and the macroscopic creep strain as function of creep time for the ACMZ alloy at 300 and 350 °C. At 300 °C and for an applied stress of 96 MPa, well into the *high-stress region*, the (211) θ′ lattice strain increases sharply with creep time (Fig. 6a), which is consistent with the results from the stepwise loading creep tests (Fig. 5). A stabilization of (211) θ′ lattice strain corresponds with the initiation of specimen necking at a creep time of ~8000 s and its eventual rupture at ~9500 s, which is reflected in the abrupt macroscopic strain increase (Fig. 6a). The (311) α-Al lattice strain experiences a slight decline with creep time as strain accumulates (Fig. 6a), which is also consistent with the stepwise loading creep tests (Fig. 4a,d and Fig. 5); this is indicative of load transfer increasing with time, as α-Al deforms plastically by creep and sheds load to the elastically-deforming θ′ precipitates. For the grain-boundary θ precipitates, both (310) and (220) orientations exhibit lattice strains that are much lower than those of α-Al, and these lattice strains remain almost unchanged with creep time. The non-negligible difference between the $(310)_\theta$ and $(220)_\theta$ peaks might reflect variations in size, location and morphology of θ precipitates contributing to these measurements. Also, θ phase has previously been found to exhibit temperature-dependent elastic anisotropy [34].

At 350 °C and for an applied stress of ~24 MPa, as shown in Fig. 6b, lattice strains of both (311) α-Al matrix and (211) θ′ intergranular precipitates are the same. This is unlike the large difference in elastic strain between these phases observed at 300 ºC and higher stress (Fig. 6a), where the ratio of lattice strains reaches a value of 3 at the onset of necking. Furthermore, at 350 °C (Fig. 6b), the α-Al and θ′ lattice strains remain nearly unchanged with creep time. Both observations indicate that very little load partitioning occurs among the two phases and is consistent with α-Al experiencing mostly elastic deformation, without much dislocation-creep-controlled plastic deformation. As the macroscopic minimum strain rate is also relatively low ($2x10^{-7}$ s^{-1}) for this condition, which is within the n~3 regime (Fig. 2b), the specimen remains unruptured even after creep time of over $4.6x10^4$ s. Lattice strains for the θ grain-boundary precipitates are also close to those of the α-Al matrix, again indicating lack of load partitioning. For the θ phase, a non-negligible difference exists for the lattice strains of the two orientations; however, unlike at 300 °C, the (310) orientation shows a lower lattice

strain than the (220) orientation. This suggests that the discrepancy in the lattice strain of different orientations is not due to an anisotropic elastic (or creep) response of θ, but rather is due to variability in location, size and/or morphology of this phase in the microstructure. For example, precipitates at grain boundaries which are oriented parallel to the loading direction might experience lower lattice strain than those on perpendicular grain boundaries.

Figures 6c,d display, for RR350 alloy at 300 and 350 °C, the evolution of (hkl) plane-specific lattice strain for α-Al (311 plane), θ′ (211 plane), and Ni-rich intermetallics (602 and 303 planes), as well as the macroscopic creep strain, as function of creep time. At 300 °C and for an applied stress of 68 MPa which corresponds to the *low-stress region*, the α-Al matrix again exhibits a constant lattice strain with creep time, as do the θ′ precipitates (beyond the primary creep regime ending at ~$2x10^4$ s, Fig. 6c); this suggests that no extensive Orowan dislocaton loops form around θ′ precipitates at this stress, as these, if formed (extensively), would cause θ′ lattice strain to increase with creep time due to increased back-stresses [18]. At 300 ºC, the (602) $Al_7Cu_2(Ni,Fe)$ lattice strains remain mostly unchanged with creep time and are nearly as high as those of the α-Al matrix (Fig. 6c), unlike the (310) θ (Al_2Cu) lattice strains (Fig. 6a) which are about half those of the α-Al matrix (Fig. 6a). This is consistent with $(310)_{\theta\text{-}Al2Cu}$ and $(602)_{AlNi}$ results shown in Fig. 5(a) at 300 ºC and confirms that the Ni-rich grain boundary phase in RR350 displays more effective load-sharing with the α-Al matrix than the θ (Al_2Cu) in ACMZ.

As shown in Fig. 6d, at 350 °C and for an applied stress of ~29 MPa (in the *n*~3 regime, Fig. 2b), the α-Al matrix lattice strain remains constant during the whole creep experiment, whereas the (211) θ′ lattice strain shows a slight decline, becoming even lower than that of α-Al near the end of the creep experiment; this is likely due to the coarsening of the θ′ precipitates. Fig. S4 shows neutron diffraction spectra acquired from the beginning, middle and end sections of the in-situ test, and the (211) θ′ peak shows no changes during creep, suggesting that its volume fraction remains unchanged during creep. Lattice strains of the Ni-rich grain-boundary phase remain constant with creep time, and for the (602) plane, the lattice strain is higher than for the α-Al matrix (Fig. 6d), whereas the (310) lattice strain for the θ grain-boundary phase in ACMZ is well below (Fig. 6b), consistent with the observations at 300 ºC (Figs. 6a,c) and the load-step experiments reported in Fig. 5(a,b).

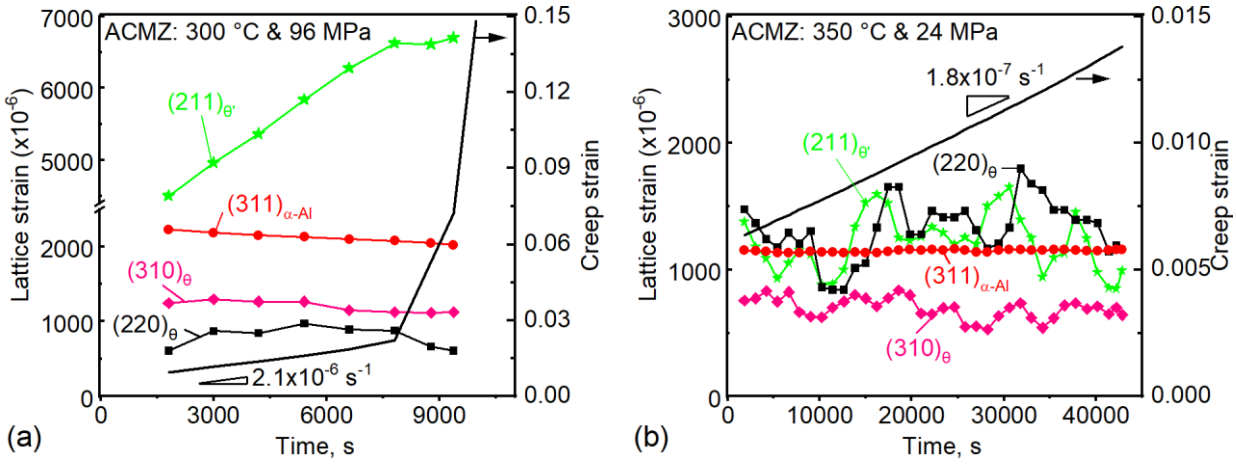

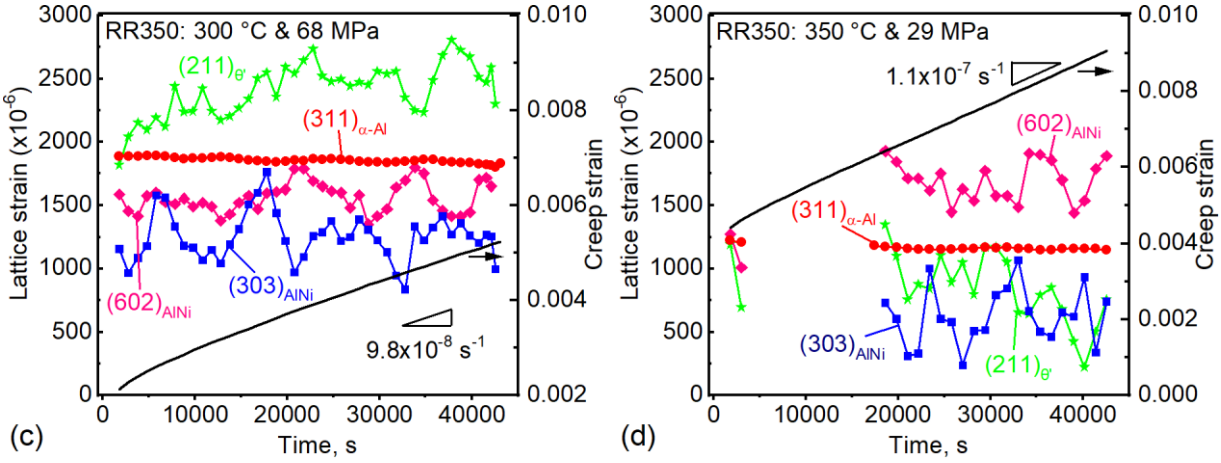

Fig. 6. Temporal evolution of the (hkl) plane-specific lattice strains for various constituent phases and macroscopic creep strain accumulating in the specimen during creep at 300 or 350 ºC, for a single stress: (a) ACMZ: 300 °C, 96 MPa (b) ACMZ: 350 °C, 24 MPa (c) RR350: 300 °C, 68 MPa (d) RR350: 350 °C, 29 MPa. Regions of missing lattice strain data in (d) are due to lack of neutron beam.

3.5 Post-creep microstructure observation

Microstructure of both RR350 and ACMZ alloys upon extensive creep exposure in the *high-stress region* has been previously characterized [3, 18]. Given that the onset of this *high-stress region* (~ 75-80 MPa, as displayed in Fig. 2a) is quite close to the yield point of the alloy at 300 °C (~ 96 MPa for RR350 when measured at strain rate of 2.5×10^{-4} s^{-1} [19]), and given the non-shearability of the θ′ precipitates [18], it is likely that, with the transition to the *high-stress region*, the Orowan looping mechanism becomes activated, thus explaining the much higher stress exponent obtained for this region as compared to the *low-stress region* (*n* value of ~24 vs. ~3, see Fig. 2a). The Orowan looping mechanism dominating the creep flow in the high-stress region for RR350 at 300 °C has been previously demonstrated [3, 18]. This conclusion was also substantiated by observation of extensive Orowan loops around θ′ precipitates [3, 18]. Due to the importance of understanding the creep behavior of θ′-strengthened Al-Cu-based alloys at stresses below their Orowan stress, microstructures of our alloys crept in the *low-stress region* are investigated using TEM, as described below.

For the RR350 alloy crept at 300 °C under an applied stress of 68 MPa, Figures 7(a) and (d) show TEM micrographs acquired close to, and away, from a grain boundary, respectively. It is apparent that θ′-precipitate-free zones (θ′-PFZ) are nearly absent (or very thin) along/near the grain boundaries of this alloy, with some matrix dislocations penetrating from the boundaries towards grain interiors (Fig. 7a). Also, dislocations pinned to the broad surfaces of face-on θ′ precipitates (indicated by arrows) residing near the grain boundaries are frequently observed, as displayed in Fig. 7a. The contrast arising from strain fields associated with dislocations pinned to θ′ precipitates is also visible for edge-on variants of precipitates (Fig. 7a). Away from grain boundaries, by contrast, matrix dislocations are still present, but at a lower density (Fig. 7d). Few dislocations pinned to θ′ precipitates can be observed in the regions away from grain boundaries (Fig. 7d). Localized dislocation creep at θ′-PFZ can increase local strain [35], leading to the dislocations bypassing some nearby θ′ precipitates by Orowan looping at even lower external stresses; but these θ′-PFZ dislocations cannot penetrate easily the grain interiors which contain θ′ precipitates, and dislocation nucleation/generation and motion away from grain boundaries are limited. Moreover, no sub-grain boundaries are observed in any of the foils studied here.

For RR350 crept at a higher temperature of 350 °C and under a lower applied stresses of 29 MPa, similar microstructural results are observed (Fig. 7b,e vs. Fig. 7a,d). While matrix dislocations are found distributed extensively near the grain boundaries, with some of them being attached to θ′ precipitates (Fig. 7b), regions far from grain boundaries are almost devoid of matrix dislocations

(Fig.7e). Dislocations pinned by θ′ precipitates or forming Orowan loops are also absent for both face-on and edge-on θ′ variants (Fig. 7e). These results suggest that, consistent with in-situ ND measurements of this alloy condition (Fig. 6d), the applied stress of 29 MPa is too low to plastically deform the interiors of the α-Al grains by the Orowan looping mechanism, consistent with the measured strain rate, which lies in the *n*~3 regime (Fig. 2b) for an applied stress below the Orowan stress; rather, plastic deformation is concentrated at/near θ′-PFZ along grain boundaries.

Turning to the ACMZ alloy, post-creep microstructures of a specimen crept at 350 °C under an applied stress of 24 MPa (Fig. 7c,f) also reveal dense matrix dislocation distribution near the grain boundaries (Fig. 7c) and their absence in the regions away from grain boundaries (Fig. 7f), again consistent with *n*~3 regime (Fig. 2b), where Orowan looping is not expected. Also, the θ′-PFZ existing along/near the grain boundaries appear to be wider for ACMZ as compared to RR350 (Fig. 7c vs. Fig. 7b), as more clearly visible in the corresponding SEM micrographs (Figs. 8a, S4a vs. Figs. 8b, S4b). The θ′-PFZ is well-developed and wider around grain-boundary θ (Al_2Cu) precipitates in ACMZ, but its presence is quite limited around Ni-rich intermetallics in RR350 (Fig. 8). Near-boundary θ′-PFZs, which are known to form during aging and subsequent heat treatments [36], widen during creep, as evidenced by the presence of small intergranular regions, found only in the post-creep microstructure of ACMZ alloy, which exhibit widespread distribution of θ and limited θ′ (Fig. S5a). Also, cracks in grain-boundary precipitates of both alloys are often observed (Fig. 8a,b), indicating that precipitates are damaged during creep, e.g., by localized grain-boundary sliding or by stress concentrations at grain triple junctions, despite the applied uniaxial stress being macroscopically compressive.

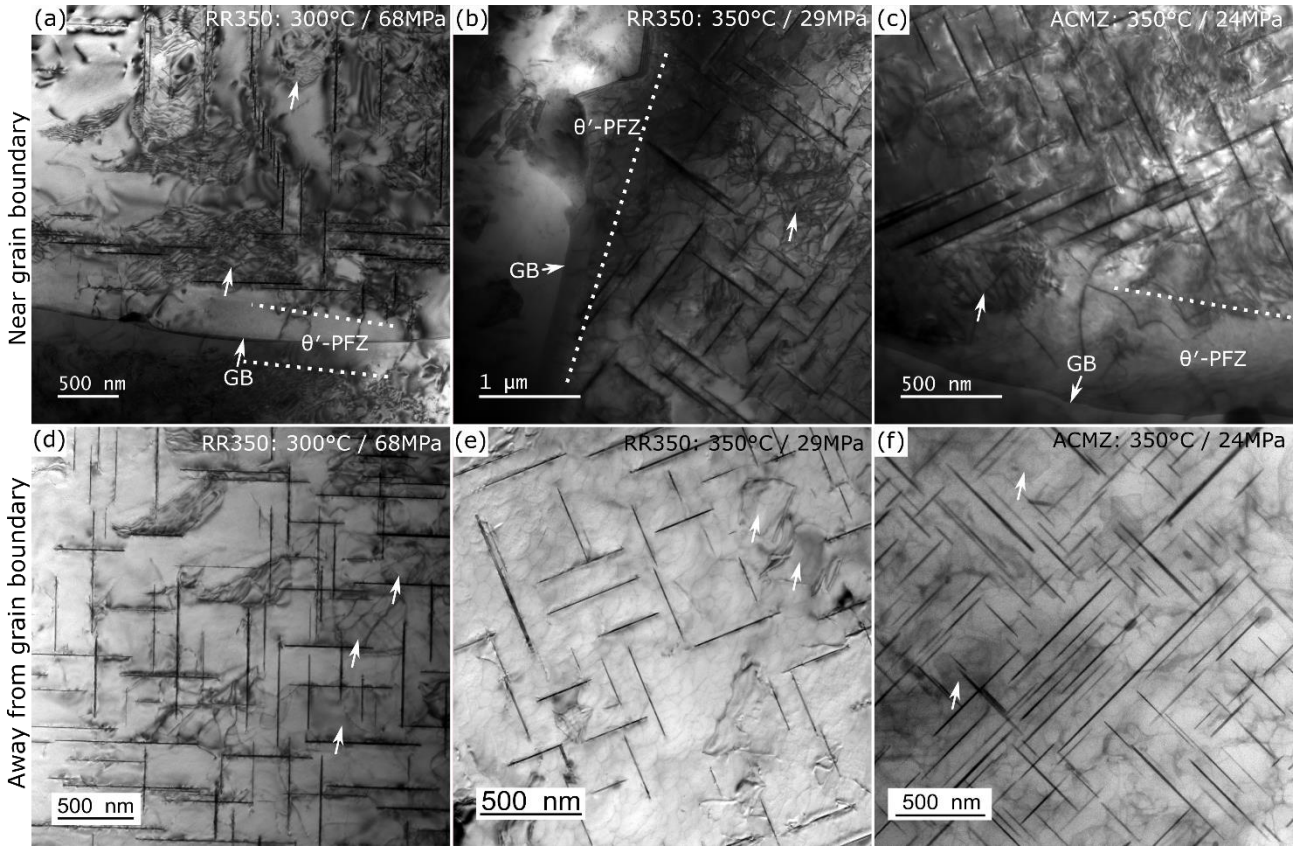

Fig. 7. Bright-field TEM micrographs, acquired along $[001]_{Al}$ zone axes, showing dislocation structures (a-c) near grain boundaries (GB) showing θ′ precipitate-free zones (θ′-PFZ). and (d-f) away from grain boundaries for (a,d) RR350 alloy crept at 300 °C with an applied stress of 68 MPa, (b,e) RR350 alloy crept at 350 °C with an applied stress

of 29 MPa and (c,f) ACMZ alloy crept at 350 °C with an applied stress of 24 MPa. Arrows indicate face-on θ′ precipitates.

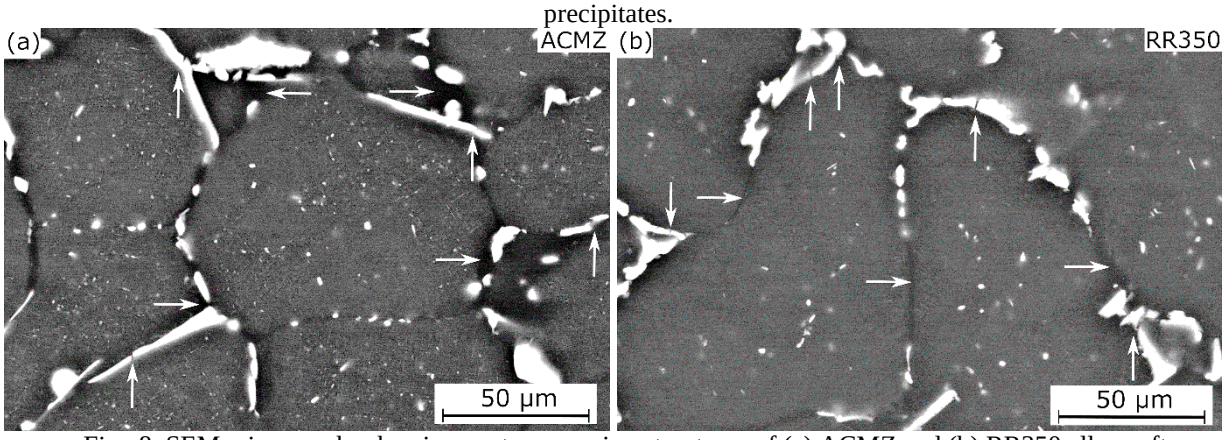

Fig. 8. SEM micrographs showing post-creep microstructures of (a) ACMZ and (b) RR350 alloys after compressive creep deformation following stepwise stress change (~15-88 MPa for ACMZ and ~15-82 MPa for RR350) at 350 °C up to a total strain of ~10%. Loading direction is vertical. Vertical arrows point to cracked grain-boundary precipitates and horizontal arrows to θ′-PFZ.

4. Discussion

4.1 Creep mechanisms at 300 °C

At 300 °C, ACMZ and RR350 exhibit three different creep regimes (Fig. 1a): (ⅰ) at low stresses (below 20-30 MPa), a diffusional creep regime (via the Coble creep mechanism) prevails, with a stress exponent n~1 [3, 19]; (ⅱ) at intermediate stresses (~20-30 MPa < σ < ~75-80 MPa), a regime exists with n~3 where an established creep mechanism is not yet identified [3]; and (ⅲ) at high stresses (above ~75-80 MPa), a n~20-25 regime is present, with Orowan looping as the dominant mechanism [3, 18]. Although the n~3 regime at intermediate stresses has been associated with the dislocation climb mechanism in Ref. [17], dislocation climb has been reasonably excluded from being a rate-limiting mechanism for such alloys in another study [18], due mostly to the high aspect ratio of θ′ precipitates. Understanding the creep mechanism at intermediate stresses (below the Orowan stress) is critical to developing new strategies to further enhance the creep resistance of θ′-strengthened Al-Cu alloys.

For stresses up to ~75-80 MPa (*low-stress region*), it is apparent that the α-Al matrix experiences little or no apparent plastic deformation originating from the Orowan looping mechanism because (ⅰ) lattice strains of both α-Al and θ′ phases increase almost linearly with stress (Fig. 5a) and almost independently of the strain accumulating in the specimen (Fig. 4a,b,d,e) and (ⅱ) matrix dislocations, if introduced during plastic deformation, would increase back-stresses from θ′ when encountering them, leading to more pronounced θ′ lattice strain increase [18], as observed in the *high-stress region* for our alloys (Fig. 5). TEM examination of RR350 crept at 300 °C at an applied stress of 67 MPa (in the *low-stress region)*, reveals numerous matrix dislocations generated at grain boundaries which penetrate towards grain interiors (Fig. 7a). Although these dislocations seem to bypass some θ′ precipitates via Orowan looping mechanism, as evidenced by the presence of Orowan loops around θ′ precipitates residing near grain boundaries (Fig. 7a), these dislocations cannot penetrate deep into grain cores, as matrix dislocations which are pinned to, or are forming Orowan loops around, θ′ precipitates are rarely seen in the TEM micrograph taken from the region away from grain boundaries (Fig. 7d). These results imply that, at intermediate stresses (n~3 regime), regions near the α-Al grain boundaries plastically deform and undergo enhanced dislocation motion during creep, but regions away from grain boundaries experience limited plastic deformation from dislocation creep. Dislocation generation is enhanced at grain boundaries due to their easy nucleation [37], and dislocation propagation can then easily occur in the θ′-PFZ adjacent to grain boundaries but not in the grain interiors where θ′ precipitates block dislocation movement because (ⅰ) the local stress is below

that to activate the Orowan looping mechanism in the grain interior, unlike in the locally weaker θ′-PFZ regions near grain boundaries (Fig. 7a,d) and (ii) dislocations, except those near the θ′ edges, cannot bypass θ′ precipitates by climb due to their high aspect ratios (Fig. 1a) [18].

However, the dislocations emitted at grain boundaries and concentrated at θ′-PFZ can lead to dislocation pipe- or core-diffusion, which in turn can promote grain-boundary sliding (GBS) [38]. The GBS occurs to prevent unfavorable crack/cavity formation at grain boundaries [30], and due to limited intragranular plastic flow, GBS can be accommodated by the activated pipe diffusion through the highly-deformed θ′-PFZ along grain boundaries [39]. Alternatively, or alongside the dislocation pipe diffusion, dislocation creep localized at θ′-PFZ may also accommodate the strain-producing GBS mechanism, by relaxing localized stress concentrations as grains slide past each other [40]. As such, the measured stress exponents, i.e., n=2.8 ± 0.2 at 300 °C and 2.7 ± 0.5 at 350 °C for Al-Cu-Mn-Zr alloys are between to n=2 regime for diffusion-controlled GBS and n=4 regime for pipe-diffusion-controlled GBS [38]. The GBS-dominated creep flow, whose rate is dependent on grain size [38], also explains why, in the n~3 regime, coarser-grained, θ′-strengthened Al-Cu-Mn-Zr alloy exhibits lower creep strain rates as compared to its finer-grained variant with the same grain-boundary precipitate volume fraction, as reported earlier [3].

4.2 Creep behavior at 350 °C

Despite the observed thermal stability of θ′ for long periods at 350 °C [10], the creep response of θ′-strengthened Al-Cu alloys has not been reported yet. Compressive creep data obtained from ex-situ tests (Fig. 2b) reveal two creep regimes with distinct stress exponents: (i) n~3 regime, for stresses up to ~55-60 MPa and (ii) n~20 regime, for stresses higher than ~55-60 MPa. These creep regimes are identical to those observed at 300 °C. Increasing temperature decreases the Orowan stress [41], and the onset of *high-stress region* (n~20 regime) is therefore associated with the activation of Orowan looping mechanism for these alloys. Similar to the n~3 regime at 300 °C, pipe-diffusion-controlled GBS may become dominant as a creep mechanism in the n~3 regime at 350 °C, consistent with (i) the measured lattice strain of θ′ which remains almost unchanged with creep time for both alloys at low stresses (n~3 regime) (Fig. 6b,d) and (ii) the absence of Orowan loops around θ′ precipitates in the regions away from grain boundaries in alloys crept at low stresses (n~3 regime) (Fig. 7e,f).

4.3 Role of grain-boundary precipitates in alloy creep performance

Given similar (θ′-dominated) microstructure in grain interiors in both RR350 and ACMZ [3], the difference in the creep performance of these two alloys at 300 and 350 °C (Fig. 2a) can be related to the distinctive features at/near their grain boundaries. Although ACMZ has slightly finer grains as compared to RR350 (43 vs. 57 μm), it has been demonstrated in a previous study [3] that an alloy with the same composition as ACMZ, but with even coarser grains (~83 μm) than RR350, continues to exhibit higher creep strain rates in all creep regimes as compared to RR350. Moreover, substantially increasing the fraction of grain-boundary θ (Al_2Cu) precipitates to ~6 vol. % in Al-Cu-Mn-Zr alloy by increasing Cu concentration beyond its solid solubility limit still produces inferior creep resistance as compared to RR350, because large θ′-PFZ volume form around θ precipitates in ACMZ [16], compared to lower θ′-PFZ volume in RR350 [3]. These results imply that the type of grain-boundary precipitates and, most importantly, the extent of θ′-PFZ around these precipitates, can exert a strong influence on both diffusional and dislocation creep rates. Observations of PFZ deteriorating alloy creep performance were also reported for Fe-Nb [42], Al-Cu-Mg [43] and 740H (Inconel) alloys [44].

Lattice strains of grain-boundary precipitates are sensitive to the applied stress during creep, as displayed in Figs. 4-6; however, Ni-rich grain-boundary precipitates in RR350 experience much

higher lattice strain increase under stress as compared to θ (Al_2Cu) grain-boundary precipitates in ACMZ. In fact, the θ lattice strain remains low, well below those of the α-Al matrix in ACMZ, whereas the lattice strains of Ni-rich precipitates in RR350 exceed those of the α-Al matrix (Fig. 5): this implies that the latter grain boundary precipitates are better suited to carry stress via load transfer from the α-Al matrix during creep deformation. However, differently-oriented Cu- and Ni-rich intermetallics in ACMZ and RR350, respectively, also exhibited different lattice strains during creep (Fig. 6), and such anisotropy may be attributable to their location at grain boundaries, residual stress changes with temperature and/or their temperature-sensitive elastic response variations along different crystallographic orientations. Moreover, unlike θ′ precipitates whose lattice strain increases with creep time in the *high-stress region* (Figs. 4 and S3) which is an indication of load transfer occurring from the plastically-deforming α-Al matrix to the elastically deforming θ′ precipitates within grains, the lattice strains of grain-boundary precipitates (both θ precipitates in ACMZ and Ni-rich precipitates in RR350) remain less affected by the creep deformation at all applied stresses. This difference is due to varying nature of precipitate – dislocation interactions. Unlike θ′ precipitates for which iso-strain condition can be assumed during creep (given their uniform distribution within α-Al grains and their high aspect ratio with nanoscale thickness and coherency with α-Al), much coarser and incoherent grain-boundary precipitates might deform in an iso-stress condition. Moreover, coarser grain-boundary precipitates tend to crack more easily (i.e., at lower applied stresses) as compared to finer precipitates [45]. Grain-boundary θ and Ni-rich intermetallics can deform elastically to remain compatible with the adjacent α-Al grains at low strains [24]; as soon as plastic strain accumulates beyond the elastic limit of these phases, local inelastic processes must occur to relax stress concentration, e.g., precipitate debonding and/or cracking, as well as plastic deformation, which all reduce the load-sharing ability of grain-boundary precipitates [45, 46]. Indeed, cracked grain-boundary precipitates are frequently observed in post-creep microstructures of both alloys (Fig. 8a,b). The θ′-PFZ near/along grain boundaries, where localization of plastic strain occurs during creep, can further promote stress relaxation mechanisms such as load shuffling back from the precipitates to the matrix [47, 48] due mostly to increased local strains [35]. Therefore, the larger θ′-PFZ volume present in ACMZ, as compared to RR350, may also explain for the lower level of load transfer, occurring from α-Al to θ precipitates in ACMZ as compared to Ni-rich precipitates in RR350.

In RR350, low θ′-PFZ volume around Ni-rich grain-boundary precipitates (Fig. 8b) is also anticipated to improve alloy creep resistance by slowing: (ⅰ) the GBS needed to accommodate diffusional creep in the n~1 regime and (ⅱ) the pipe-diffusion-controlled GBS (the mechanism expected to be operative in the n~3 and other creep regimes). In ACMZ, by contrast, wide continuous θ′-PFZ with high dislocation density are formed, due to localized dislocation creep flow, which can accelerate pipe-diffusion-controlled GBS as discussed in Section 4.1. Moreover, larger volume of θ′-PFZ where localized dislocation creep flow occurs can increase overall creep strain rate of the alloy [3, 49] which, along with the expected higher GBS rate, explain the higher creep strain rates observed for ACMZ as compared to RR350 in the *n*~3 regime.

4.4 Modeling of lattice strain evolution determined from in-situ neutron diffraction creep tests

As noted earlier, in RR350 and ACMZ alloys, the precipitates within grain interiors are similar, unlike those present at grain boundaries. A recent model [24, 34] has successfully captured the lattice strain evolution in the θ′ precipitates as a function of macrostrain when Orowan looping is the primary mechanism by which dislocations bypass precipitates. The model assumes that θ′ precipitates, due to their high aspect ratio, do not accommodate shear stresses and rotate as a response to shear deformation. The input parameters to the model are the tensile stress and macroscopic strain response during the creep test, as well as the volume fraction of θ′ precipitate in the alloy. Model predictions

and experimental measurements for the (211) θ′ precipitate lattice strain evolution as a function of creep macrostrain at 300 °C are presented in Fig. 9 for RR350 (Figs. 9a-b) and ACMZ (Figs. 9c-d) alloys. Good correspondence between the model and neutron diffraction data exists for the RR350 alloy (Figs. 9a-b), supporting the hypothesis that the macroscopic creep strain is effectively transferred to the θ′ precipitates in the grain interiors for the range of stresses where a stress exponent n=20-24 is obtained (Fig. 2a). These predictions for the RR350 alloy are further consistent with microscopic results presented above and in previous studies [3, 18]; thus, Orowan looping is the bypass mechanism for the dislocations in the bulk of the grains in this alloy and the dominant creep mechanism in the alloy at high stresses (> 75-80 MPa). The ACMZ alloy lattice strain model predictions and measured values, however, indicate a discrepancy. The model-predicted lattice strain values are higher than the strain values measured by in-situ neutron diffraction, by a factor of two to three (Fig. 9c-d). This implies that the measured creep macrostrain is accommodated elsewhere in the microstructure. It is likely that creep deformation in the well-developed θ′-PFZ regions of the ACMZ alloy (Fig. 1b) is responsible for the disagreement between the predicted and modeled lattice strain. Grain-boundary microstructure, therefore, has a direct bearing on the deformation of the grain bulk, even in the power-law creep regime. While the presented approach can be applied to further discretize the macroscopic creep deformation between grain boundary and grain bulk regions, we leave that for future work.

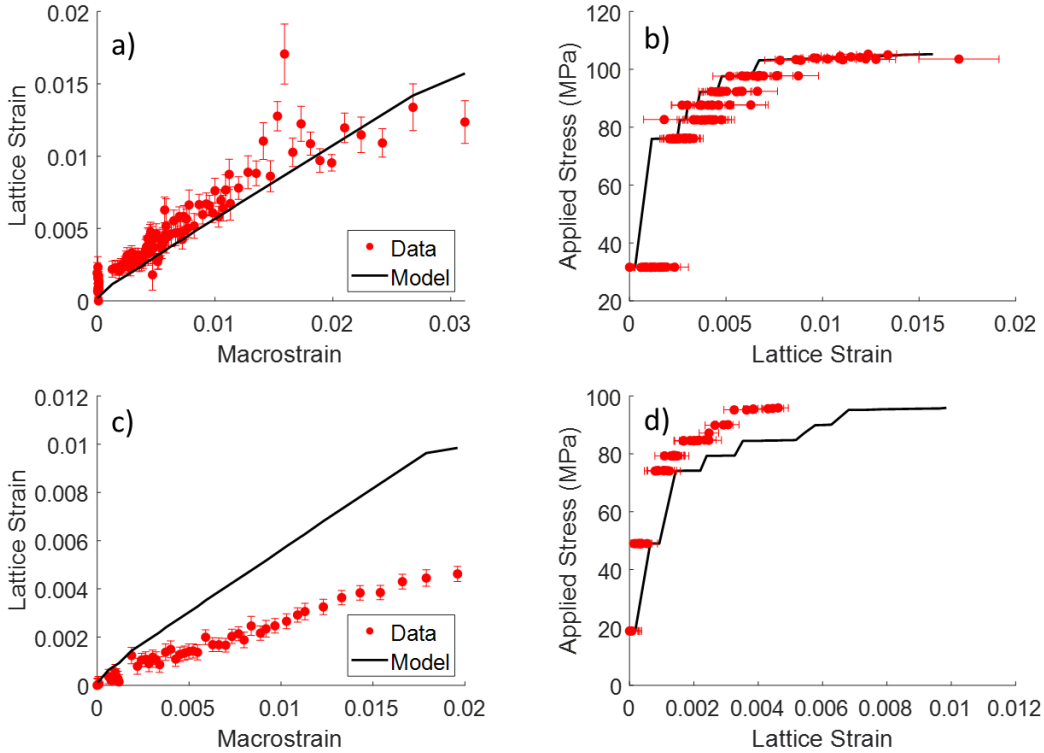

Fig. 9. Comparison of modeling results with measured (211) lattice strain in the θ′ precipitates for in-situ creep tests conducted at 300 °C and under the applied stresses above 75 MPa: (a,c) modeled and measured lattice strain as a function of creep macrostrain for (a) RR350 and (c) ACMZ; (b,d) modeled and measured lattice strain evolution as a function of the applied stress in multi-step loading creep tests at 300 °C for (b) RR350 and (d) ACMZ alloys.

4.5 Implications of grain boundary particle chemistry and load-sharing for alloy design

Formation of higher volumes of θ′-PFZ in ACMZ as compared to RR350 reflects the different types of grain-boundary precipitates: Cu-rich θ-Al_2Cu in ACMZ and Ni- and Fe-containing phases (Al_7Cu_2(Ni,Fe) and Al_9NiFe) in RR350. The latter phases are expected to be much more coarsening-resistant than θ-Al_2Cu, given the much slower diffusivity and lower solid solubility of Ni and Fe, as

compared to Cu, in α-Al at 300 and 350 °C [14]. Also, grain-boundary θ-Al_2Cu precipitates form at grain boundaries during aging alongside coarser θ-precipitates formed earlier during solidification; both tend to coarsen at the expense of nearby θ′-Al_2Cu precipitates in the grains, thus leading to widened θ′-PFZ during preconditioning and creep (Figs. 8a, S4a), unlike the Ni-containing intermetallic phases which are not expected to consume θ′-Al_2Cu precipitates during their coarsening, consistent with the limited/absence of θ′-PFZ around Ni-rich intermetallics (Fig. 8b).

The results of this study imply that, when dislocation-driven deformation in α-Al grain interiors is inhibited, the grain-boundary precipitates and the volume of θ′-PFZ at/along grain boundaries become essential parameters in controlling alloy creep performance. Coarsening-resistant intermetallic phases enriched with slow-diffusers at grain boundaries will minimize θ′-PFZ formation and enhance both load sharing and suppression of (pipe-diffusion-controlled and/or dislocation-controlled) GBS. Moreover, various types of coarsening-resistant grain-boundary precipitates, owing to their different interfacial structures with α-Al, can have distinctive effects on θ′-PFZ formation and the resulting creep strain rates.

5. Conclusions

Creep mechanisms prevailing at 300 and 350 °C in two θ′ (metastable Al_2Cu)-strengthened alloys - Al-Cu-Mn-Zr (labeled ACMZ) and Al-Cu-Mn-Zr-Ni-Co-Sb (labeled RR350) – and the influence of grain-boundary precipitates on their creep performance have been explored by utilizing (ⅰ) in-situ neutron diffraction measurements during creep, (ⅱ) additional compressive creep experiments performed ex-situ (without ND diffraction) and (ⅲ) pre- and post-creep microstructure investigations. The following conclusions can be drawn:

- At high stresses (>75-80 MPa at 300 °C and >55-60 MPa at 350 °C), both ACMZ and RR350 exhibit very high creep stress exponent (n~20-25), with Orowan looping the rate-limiting mechanism. This is evidenced by a decreasing α-Al lattice strain in response to linearly increasing θ′ lattice strain with strain accumulation at any given stress, which is indicative of increasing load transfer from plastically-deforming α-Al to elastically-deforming θ′ with the accumulation of more Orowan loops around θ′ precipitates.

- At lower stresses (<75-80 MPa at 300 °C and <55-60 MPa at 350 °C), both ACMZ and RR350 exhibit a creep regime with a moderate stress exponent (n~3), with both α-Al and θ′ lattice strains increasing almost linearly with applied stress and remaining unaffected with strain accumulation, which indicates that Orowan looping or dislocation pile-up around θ′ is inactive within the grains. Dislocation climb mechanism is also limited given the high aspect ratio of highly non-shearable θ′ precipitates. TEM observations of crept alloys also confirm limited dislocation mobility and Orowan loops around θ′ within α-Al grains. Based on the stress exponent (n~3) and the high dislocation concentration at/near precipitate-free zones (θ′-PFZ) along grain boundaries, a grain-boundary sliding (GBS) mechanism - controlled by localized pipe diffusion and/or dislocation flow at θ′-PFZ - is proposed as the rate-limiting creep mechanism in this n~3 regime.

- Compared to θ′ precipitates in the α-Al grains, to which load transfer occurs effectively from the plastically-deforming α-Al matrix, grain-boundary precipitates (θ-Al_2Cu in ACMZ and Ni-rich intermetallic phases in RR350) exhibit a much lower load-sharing effect. However, grain-boundary precipitates share load with α-Al matrix more effectively in RR350 than in ACMZ. This is, in part, attributed to the presence of wider θ′-PFZ (where localized dislocation creep occurs even at low applied stresses) around grain-boundary θ-Al_2Cu as compared to Ni-rich intermetallics, which can accelerate their plastic relaxation by cracking during creep.

Wider θ′-PFZ in ACMZ as compared to RR350 increases strain rates in (i) the diffusional (n~1) creep regime, which is controlled by the Coble mechanism (i.e., vacancy diffusion along grain boundaries), and (ii) the GBS-dominated (n~3) regime, which is hypothesized to be controlled by dislocation pipe diffusion and/or dislocation flow along grain boundaries. Close agreement is found between model predictions and experimental measurements for the (211) θ′ lattice strain evolution as function of macrostrain for RR350. However, for ACMZ, substantial deviations exist between model and experiments, consistent with macrostrain accumulation occurring along grain boundaries with well-developed θ′-PFZ.

- Limited θ′-PFZ volumes around Ni-rich phases at grain boundaries is attributable to the excellent coarsening resistance of Ni-rich intermetallics at 300 and 350 °C (reflecting the very low diffusivity and solubility of Ni in α-Al at these temperatures). By contrast, θ-Al_2Cu grain-boundaries precipitates experience coarsening during both preconditioning and creep at the expense of nearby θ′ precipitates, leading to the formation of wider θ′-PFZ around θ and along grain boundaries.

Acknowledgements – JUR and DCD acknowledge funding from Oak Ridge National Laboratory via contract # 4000182026. This research was sponsored by the Powertrain Materials Core Program, under the Propulsion Materials Program (managed by Jerry Gibbs), Vehicle Technologies Office, US Department of Energy (DOE). A portion of this research used resources at Oak Ridge National Laboratory's Spallation Neutron Source, sponsored by the Scientific User Facilities Division, Office of Basic Energy Sciences, U.S. Department of Energy. Drs. David Hoelzer and Christopher Fancher at Oak Ridge National Laboratory are acknowledged for reviewing and providing useful feedback on this manuscript.

Conflict of interest – DCD discloses a financial interest in NanoAl, LLC (part of Steel Dynamics Inc.) which is active in cast aluminum alloys.

References

[1] U. Bansal, M.P. Singh, S. Mondol, S.K. Sinha, S.K. Makineni, A. Paul, K. Chattopadhyay, The interplay of precipitation of ordered compounds and interfacial segregation in Al-Cu-Hf-Si alloys for high-temperature strength, Acta Mater. 240 (2022) 118355.
[2] B. Gwalani, J. Liu, S. Lambeets, M. Olszta, J. Poplawsky, A. Shyam, A. Devaraj, Rapid assessment of interfacial stabilization mechanisms of metastable precipitates to accelerate high-temperature Al-alloy development, Mater Res Lett 10(12) (2022) 771-779.
[3] J.U. Rakhmonov, S. Bahl, A. Shyam, D.C. Dunand, Cavitation-resistant intergranular precipitates enhance creep performance of θ′-strengthened Al-Cu based alloys, Acta Mater. 228 (2022) 117788.
[4] P. Shower, J. Poplawsky, S. Bahl, A. Shyam, The role of Si in determining the stability of the θ′ precipitate in Al-Cu-Mn-Zr alloys, J. Alloys Compd. 862 (2021) 158152.
[5] L. Jiang, B. Rouxel, T. Langan, T. Dorin, Coupled segregation mechanisms of Sc, Zr and Mn at θ′ interfaces enhances the strength and thermal stability of Al-Cu alloys, Acta Mater. 206 (2021) 116634.
[6] J.D. Poplawsky, B.K. Milligan, L.F. Allard, D. Shin, P. Shower, M.F. Chisholm, A. Shyam, The synergistic role of Mn and Zr/Ti in producing θ′/L12 co-precipitates in Al-Cu alloys, Acta Mater. 194 (2020) 577-586.
[7] Y.H. Gao, C. Yang, J.Y. Zhang, L.F. Cao, G. Liu, J. Sun, E. Ma, Stabilizing nanoprecipitates in Al-Cu alloys for creep resistance at 300°C, Mater Res Lett 7(1) (2019) 18-25.
[8] D. Li, K. Liu, J. Rakhmonov, X.G. Chen, Enhanced thermal stability of precipitates and elevated-temperature properties via microalloying with transition metals (Zr, V and Sc) in Al–Cu 224 cast alloys, Materials Science and Engineering: A 827 (2021) 142090.

[9] J. Rakhmonov, K. Liu, L. Pan, F. Breton, X.G. Chen, Enhanced mechanical properties of high-temperature-resistant Al–Cu cast alloy by microalloying with Mg, J. Alloys Compd. 827 (2020) 154305.
[10] A. Shyam, S. Roy, D. Shin, J.D. Poplawsky, L.F. Allard, Y. Yamamoto, J.R. Morris, B. Mazumder, J.C. Idrobo, A. Rodriguez, T.R. Watkins, J.A. Haynes, Elevated temperature microstructural stability in cast AlCuMnZr alloys through solute segregation, Materials Science and Engineering: A 765 (2019) 138279.
[11] S. Bahl, L. Xiong, L.F. Allard, R.A. Michi, J.D. Poplawsky, A.C. Chuang, D. Singh, T.R. Watkins, D. Shin, J.A. Haynes, A. Shyam, Aging behavior and strengthening mechanisms of coarsening resistant metastable θ' precipitates in an Al–Cu alloy, Mater Design 198 (2021) 109378.
[12] S. Roy, L.F. Allard, A. Rodriguez, W.D. Porter, A. Shyam, Comparative Evaluation of Cast Aluminum Alloys for Automotive Cylinder Heads: Part II-Mechanical and Thermal Properties, Metall. Mater. Trans. A 48A(5) (2017) 2543-2562.
[13] R.A. Michi, A. Plotkowski, A. Shyam, R.R. Dehoff, S.S. Babu, Towards high-temperature applications of aluminium alloys enabled by additive manufacturing, Int. Mater. Rev. (2021) 1-48.
[14] J. Rakhmonov, G. Timelli, F. Bonollo, The Effect of Transition Elements on High-Temperature Mechanical Properties of AlSi Foundry AlloysA Review, Adv. Eng. Mater. 18(7) (2016) 1096-1105.
[15] K.E. Knipling, D.C. Dunand, D.N. Seidman, Criteria for developing castable, creep-resistant aluminum-based alloys - A review, International Journal of Materials Research 97(3) (2006) 246-265.
[16] S. Bahl, J.U. Rakhmonov, C. Kenel, D.C. Dunand, A. Shyam, Effect of grain-boundary θ-Al2Cu precipitates on tensile and compressive creep properties of cast Al–Cu–Mn–Zr alloys, Materials Science and Engineering: A 840 (2022) 142946.
[17] P. Hu, K. Liu, L. Pan, X.G. Chen, Effect of Mg microalloying on elevated-temperature creep resistance of Al–Cu 224 cast alloys, Materials Science and Engineering: A (2022) 143649.
[18] B. Milligan, D. Ma, L. Allard, A. Clarke, A. Shyam, Dislocation-θ' (Al2Cu) interactions during creep deformation of an Al-Cu alloy, Scripta Mater. 217 (2022) 114739.
[19] B.K. Milligan, S. Roy, C.S. Hawkins, L.F. Allard, A. Shyam, Impact of microstructural stability on the creep behavior of cast Al–Cu alloys, Materials Science and Engineering: A 772 (2020) 138697.
[20] D.-K. Kim, W. Woo, J.-H. Hwang, K. An, S.-H. Choi, Stress partitioning behavior of an AlSi10Mg alloy produced by selective laser melting during tensile deformation using in situ neutron diffraction, J. Alloys Compd. 686 (2016) 281-286.
[21] R. Vaidyanathan, M.A.M. Bourke, D.C. Dunand, Analysis of neutron diffraction spectra acquired in situ during stress-induced transformations in superelastic NiTi, J. Appl. Phys. 86(6) (1999) 3020-3029.
[22] S. Ma, D. Brown, M.A.M. Bourke, M.R. Daymond, B.S. Majumdar, Microstrain evolution during creep of a high volume fraction superalloy, Materials Science and Engineering: A 399(1) (2005) 141-153.
[23] H.M.A. Winand, A.F. Whitehouse, P.J. Withers, An investigation of the isothermal creep response of Al-based composites by neutron diffraction, Materials Science and Engineering: A 284(1) (2000) 103-113.
[24] B. Milligan, D. Ma, L. Allard, A. Clarke, A. Shyam, Crystallographic orientation-dependent strain hardening in a precipitation-strengthened Al-Cu alloy, Acta Mater. 205 (2021) 116577.
[25] K. An, H.D. Skorpenske, A.D. Stoica, D. Ma, X.-L. Wang, E. Cakmak, First In Situ Lattice Strains Measurements Under Load at VULCAN, Metall and Mat Trans A 42(1) (2011) 95-99.
[26] S. Ma, P. Rangaswamy, B.S. Majumdar, Microstress evolution during in situ loading of a superalloy containing high volume fraction of γ' phase, Scripta Mater. 48(5) (2003) 525-530.
[27] H.E. Gresham, L. Eaton, A.G. Farnsworth, Aluminum base alloy, in: U.S.p. office (Ed.) Rolls-Royce Limited, Great Britain, 1957.
[28] O. Golan, A. Arbel, D. Eliezer, D. Moreno, The applicability of Norton's creep power law and its modified version to a single-crystal superalloy type CMSX-2, Materials Science and Engineering: A 216(1) (1996) 125-130.
[29] A.M. Jansen, D.C. Dunand, Creep of metals containing high volume fractions of unshearable dispersoids—Part II. Experiments in the Al□Al2O3 system and comparison to models, Acta Mater. 45(11) (1997) 4583-4592.
[30] M.E. Kassner, M.T. Pérez-Prado, Five-power-law creep in single phase metals and alloys, Prog. Mater Sci. 45(1) (2000) 1-102.

[31] V. Vaithyanathan, C. Wolverton, L.Q. Chen, Multiscale modeling of theta ' precipitation in Al-Cu binary alloys, Acta Mater. 52(10) (2004) 2973-2987.
[32] S. Harjo, N. Tsuchida, J. Abe, W. Gong, Martensite phase stress and the strengthening mechanism in TRIP steel by neutron diffraction, Sci Rep-Uk 7(1) (2017) 15149.
[33] P.T. Summers, Y. Chen, C.M. Rippe, B. Allen, A.P. Mouritz, S.W. Case, B.Y. Lattimer, Overview of aluminum alloy mechanical properties during and after fires, Fire Science Reviews 4(1) (2015) 3.
[34] W.F. Hosford, R.H. Zeisloft, The anisotropy of age-hardened Al-4 pct Cu single crystals during plane-strain compression, Metallurgical and Materials Transactions B 3(1) (1972) 113-121.
[35] T. Krol, D. Baither, E. Nembach, The formation of precipitate free zones along grain boundaries in a superalloy and the ensuing effects on its plastic deformation, Acta Mater. 52(7) (2004) 2095-2108.
[36] M.M. Arani, N.S. Ramesh, X. Wang, N. Parson, M. Li, W.J. Poole, The localization of plastic deformation in the precipitate free zone of an Al-Mg-Si-Mn alloy, Acta Mater. 231 (2022) 117872.
[37] R.B. Nicholson, G. Thomas, J. Nutting, The interaction of dislocations and precipitates, Acta Metall. 8(3) (1960) 172-176.
[38] O.A. Ruano, O.D. Sherby, On constitutive equations for various diffusion-controlled creep mechanisms, Rev. Phys. Appl. 23(4) (1988) 625-637.
[39] J.H. Ree, Grain boundary sliding and development of grain boundary openings in experimentally deformed octachloropropane, Journal of Structural Geology 16(3) (1994) 403-418.
[40] J. Cadek, Creep in metallic materials, Elsevier, New York, 1998.
[41] 6 - Creep of Second Phase Particles Strengthened Materials, in: J.-S. Zhang (Ed.), High Temperature Deformation and Fracture of Materials, Woodhead Publishing2010, pp. 83-101.
[42] J.A. Wert, E.R. Parker, V.F. Zackay, Elimination of precipitate free zones in an Fe−Nb creep-resistant alloy, Metall. Trans. A 10(9) (1979) 1313-1322.
[43] X. Wu, L. Zhan, C. Guan, X. Yang, J. He, Effect of creep aging parameters on creep resistance behavior of Al–Cu–Mg alloy, Materials Research Express 6(12) (2019) 1265a7.
[44] D.H. Bechetti, J.N. DuPont, J.J. de Barbadillo, B.A. Baker, M. Watanabe, Microstructural Evolution of INCONEL® Alloy 740H® Fusion Welds During Creep, Metall and Mat Trans A 46(2) (2015) 739-755.
[45] X. Hu, S. Bahl, A. Shyam, A. Plotkowski, B. Milligan, L. Allard, J.A. Haynes, Y. Ren, A. Chuang, Repurposing the θ (Al2Cu) phase to simultaneously increase the strength and ductility of an additively manufactured Al–Cu alloy, Materials Science and Engineering: A 850 (2022) 143511.
[46] S. Huang, D.W. Brown, B. Clausen, Z. Teng, Y. Gao, P.K. Liaw, In Situ Neutron-Diffraction Studies on the Creep Behavior of a Ferritic Superalloy, Metall and Mat Trans A 43(5) (2012) 1497-1508.
[47] T.F. Morgeneyer, M.J. Starink, S.C. Wang, I. Sinclair, Quench sensitivity of toughness in an Al alloy: Direct observation and analysis of failure initiation at the precipitate-free zone, Acta Mater. 56(12) (2008) 2872-2884.
[48] R.A. Michi, S. Bahl, C.M. Fancher, K. Sisco, L.F. Allard, K. An, D. Yu, R.R. Dehoff, A. Plotkowski, A. Shyam, Load shuffling during creep deformation of an additively manufactured AlCuMnZr alloy, Acta Mater. 244 (2023) 118557.
[49] B. Wilshire, M.T. Whittaker, The role of grain boundaries in creep strain accumulation, Acta Mater. 57(14) (2009) 4115-4124.

Supplementary information

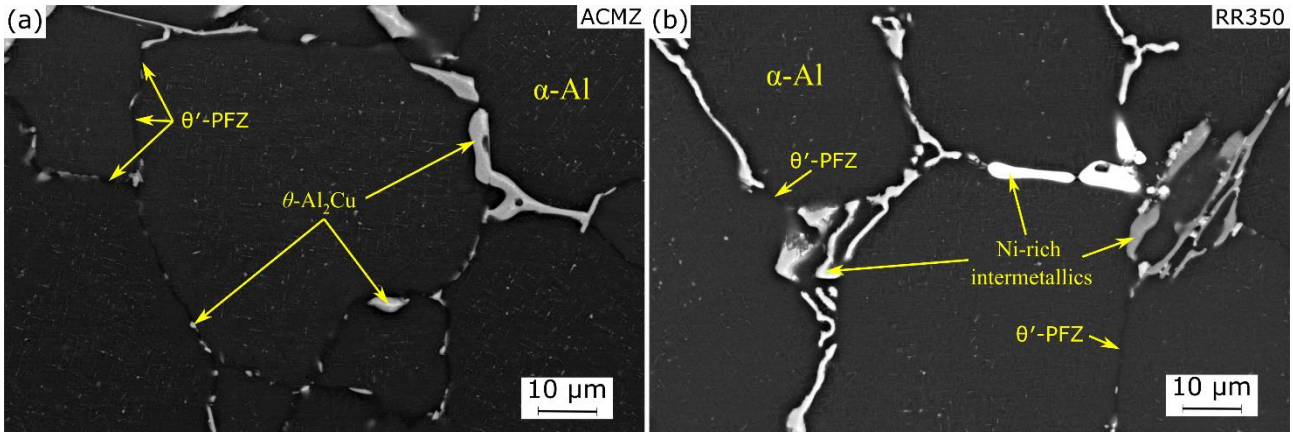

Fig. S1. Low-magnification SEM micrographs showing microstructures of (a) ACMZ and (b) RR350 alloys after preconditioning heat treatment at 300 °C for 200 h and prior to creep.

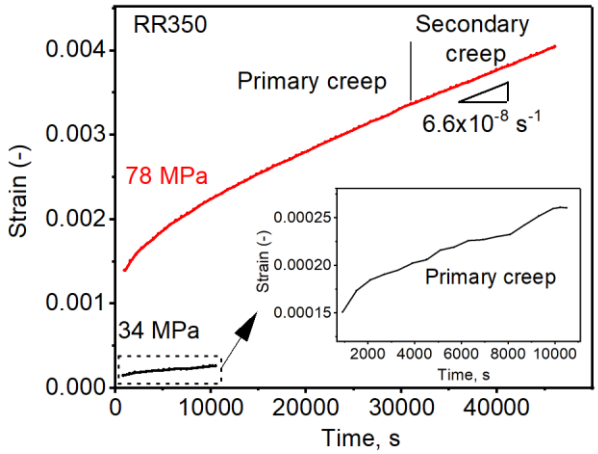

Fig. S2. Temporal evolution of creep strain for applied stresses of 34 and 78 MPa for RR350 tested in-situ at 300 °C. Primary and secondary creep regimes are indicated.

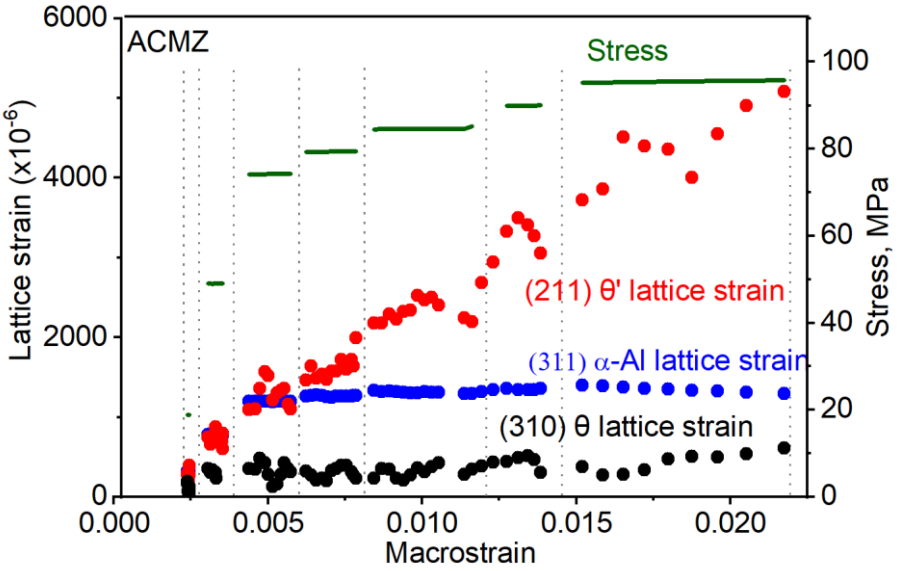

Fig. S3. Evolution of (hkl) plane-specific lattice strains of α-Al, θ′ and θ phases as function of macrostrain accumulating in ACMZ alloy specimen at various applied stresses during in-situ tensile creep at 300ºC.

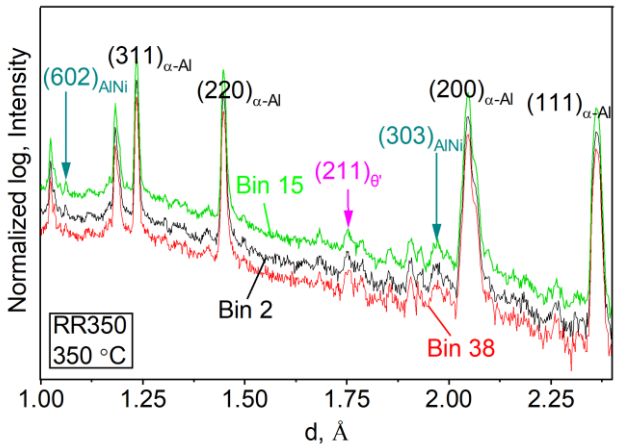

Fig. S4. Neutron diffraction spectra acquired during tensile creep of RR350 alloy at 350 °C and under 29 MPa constant stress. Bins 2, 15 and 38 correspond to the beginning, middle and end sections of the in-situ creep test.

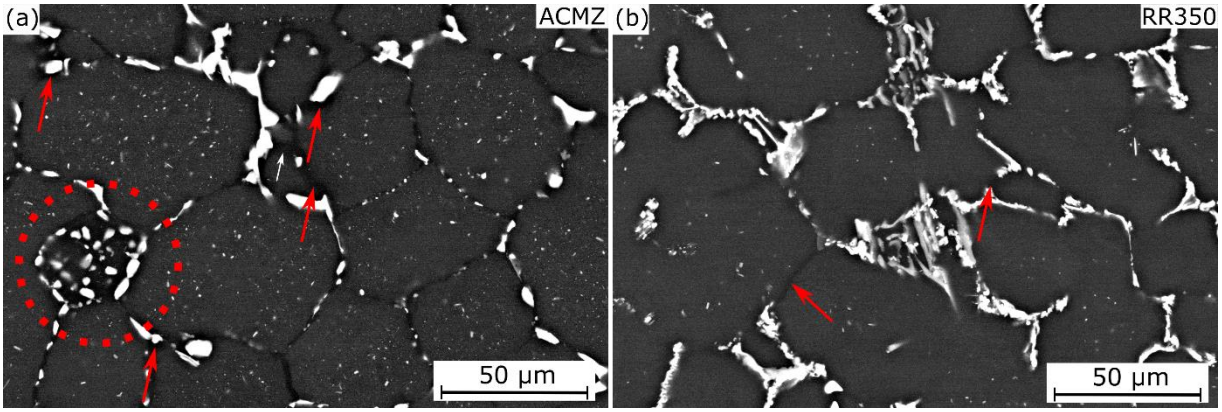

Fig. S5. Low-magnification SEM micrographs showing post-creep microstructures of (a) ACMZ and (b) RR350 alloys crept in compression during multi-step loading creep (~15-88 MPa for ACMZ and ~15-82 MPa for RR350) at 350 °C up to a total strain of ~10%. Shown within the circled area in (a) is a small region in ACMZ, where fine intragranular θ′ precipitates transformed into coarser θ precipitates during creep. Loading direction is vertical. Arrows point to θ′-PFZ.

Graphical abstract